polymers

MDPI

Article

Biodegradable Polymeric Foams Based on Modified Castor Oil, Styrene, and Isobornyl Methacrylate

James Anthony Dicks * and Chris Woolard

Centre for Materials Engineering, Department of Mechanical Engineering, University of Cape Town, Cape Town 7701, South Africa; chris.woolard@uct.ac.za
* Correspondence: james.anthony.dicks@gmail.com

Abstract: The environmental issues of petroleum-derived polymeric foams have necessitated seeking renewable alternatives. This work aims to prepare renewable free-radically polymerized polymeric foams with the ability to biodegrade. Furthermore, this work attempted to incorporate a bio-based reactive diluent, which has not been reported in the literature. The synthesis of maleated castor oil glycerides was performed with products analyzed by Fourier transform infrared spectrometry using attenuated total reflection (ATR-FTIR) and ^{1}H nuclear magnetic resonance (^{1}H NMR) spectroscopy. Polymeric foams were prepared using maleated castor oil glycerides via free radical copolymerization with styrene and isobornyl methacrylate as reactive diluents. Scanning electron microscopy (SEM) was used to determine anisotropic macrocellular morphology, with log-normal cell diameter distributions. The compressive mechanical and energy absorption properties were investigated; the polymeric foams displayed Young's modulus up to 26.85 ± 1.07 MPa and strength up to 1.11 ± 0.021 MPa using styrene as the reactive diluent, and Young's modulus up to 1.38 ± 0.055 MPa and strength up to 0.088 MPa when incorporating isobornyl methacrylate. Furthermore, a thorough analysis of the cellular structure–property relationships was performed, indicating relationships to cell diameter, cell wall thickness and apparent density. The polymeric foams displayed rapid mass loss in an aerobic soil environment with multiple erosion sites revealed by SEM. In conclusion, renewable polymeric foams with excellent compressive properties were achieved using styrene as reactive diluent, but the incorporation of isobornyl methacrylate decreased strength-related properties.

Keywords: vegetable oil; polymeric foam; castor oil; reactive diluent; isobornyl methacrylate; renewable; biodegradable

check for updates

Citation: Dicks, J.A.; Woolard, C. Biodegradable Polymeric Foams Based on Modified Castor Oil, Styrene, and Isobornyl Methacrylate. *Polymers* **2021**, *13*, 1872. https://doi.org/10.3390/polym13111872

Academic Editors: José Ignacio Velasco and Marcelo Antunes

Received: 19 May 2021
Accepted: 1 June 2021
Published: 4 June 2021

Publisher's Note: MDPI stays neutral with regard to jurisdictional claims in published maps and institutional affiliations.

Copyright: © 2021 by the authors. Licensee MDPI, Basel, Switzerland. This article is an open access article distributed under the terms and conditions of the Creative Commons Attribution (CC BY) license (https://creativecommons.org/licenses/by/4.0/).

1. Introduction

In response to environmental concerns surrounding petroleum-derived polymeric materials several renewable thermosetting alternatives have been developed. A primary feedstock of these alternatives is vegetable oils (VOs) [1–9]. The functionalization of VOs to prepare thermosetting polymers through free radical polymerization has been developed for several years. A range of both VOs (e.g., soybean, linseed, tung, and castor oils) and functionalization strategies (e.g., epoxidation, acrylation, methacrylation, and maleation) were employed. However, the use of these modified VOs to prepare polymeric foams has remained relatively limited. Of the polymeric foams prepared using modified VOs, acrylated epoxidized soybean oil (AESO) has received the most attention [10–17]. In the case of AESO-based polymeric foams, either homopolymerization or copolymerization with styrene as a reactive diluent was performed. The use of small, rigid compounds as reactive diluents, e.g., styrene, can be useful to provide hard segments within the polymer matrix, thus increasing its mechanical properties. On the other hand, the use of styrene decreases the bio-based carbon content of the product, which is a volatile organic compound, hazardous air pollutant, and a potential human carcinogen [18,19]. While various bio-based reactive diluents have been developed and employed in VO-derived

polymeric materials, to the best of the authors' knowledge these compounds have yet to be introduced into VO-derived free radically polymerized polymeric foams [20,21]. Isobornyl methacrylate (IBOMA) was identified as a promising candidate as a bio-based reactive diluent due to its fused bicyclic ring that could contribute hard segments to the polymer matrix, and due to its low cost, high bio-based carbon content, and commercial availability.

Efforts by Wang and coworkers [22,23] demonstrated the use of maleated castor oil (MACO) to prepare polymeric foams with styrene as a reactive diluent. Castor oil triglycerides provide a reliable feedstock of high purity fatty acid content (~90% ricinoleic acid moieties), which contain secondary hydroxyl functionality at the C_9 position. The hydroxyl functionality provided a convenient platform for facile, solvent-free, high-yield acid anhydride esterification with maleic anhydride to produce suitable sites for free radical copolymerization with styrene. Furthermore, the carboxylic acid groups present on the maleate half esters provided convenient functionality for acid-metal carbonate reaction with sodium hydrogen carbonate ($NaHCO_3$) to induce foaming through CO_2 liberation as a byproduct. Several studies have demonstrated the improved mechanical properties of polymers prepared with maleated castor oil glycerides (MACOG), a mixture of maleated mono- and diglycerides, compared to that of MACO [18,24–28]. Indeed, it could be expected that reducing the content of long, flexible fatty acid chains per molecule should improve the strength-related properties and T_g. This work therefore aims to assess whether the use of MACOG could be a suitable modified VO for the preparation of semi-rigid polymeric foams. This work also aimed to incorporate isobornyl methacrylate (IBOMA) as a bio-based reactive diluent and to assess whether it was a suitable alternative to petroleum-derived reactive diluents such as styrene. Furthermore, an in-depth analysis of the structure–property relationships and energy absorption properties was sought to gain a deeper understanding of the cellular mechanics and provide a basis for product design suitability, which is often lacking in the literature for bio-based polymeric foams.

2. Materials and Methods

2.1. Materials

Castor oil (B.P. grade) was purchased from a local pharmacy (Dischem, Cape Town, South Africa). Isobornyl methacrylate (IBOMA, technical grade, stabilized with 150 ppm monomethyl ether hydroquinone), styrene (≥99%, stabilized with 4-tert-butylcatechol), glycerol (98%), $Ca(OH)_2$ (≥95%), maleic anhydride (MA, 99%), sodium hydrogen carbonate ($NaHCO_3$, 99.7%), sodium hydroxide (99.5%), hydroquinone (98%), *N*,*N*-dimethylaniline (*N*,*N*-DMA, ≥99%), *N*,*N*-dimethylbenzylamine (*N*,*N*-DMBA, ≥99%), dibenzoyl peroxide (BPO, Luperox A75), surfactant (Ewopal 80), diethyl ether (99%), toluene (99.5%) were purchased from Sigma Aldrich (Modderfontein, South Africa). Oxalic acid, sodium hydroxide, ethanol (99.6%), and anhydrous $MgSO_4$ were supplied by Kimix Chemicals, Cape Town, South Africa. Styrene contained 4-tert-butylcatechol stabilizer, which was removed by washing with 2M NaOH twice, followed by sequential washing with distilled water and a 4 wt% NaCl aqueous solution. The product was then dried over anhydrous $MgSO_4$ and filtered. All other materials were used as received.

2.2. Synthesis of Castor Oil Glycerides and Maleated Castor Oil Glycerides

The synthesis of castor oil glycerides and maleation of castor oil glycerides was performed by a two-step, "one-pot" synthesis (Figure 1), which was similar to that reported elsewhere [18,24,28]. Details of the syntheses and product characterization can be found in the Supplementary Materials.

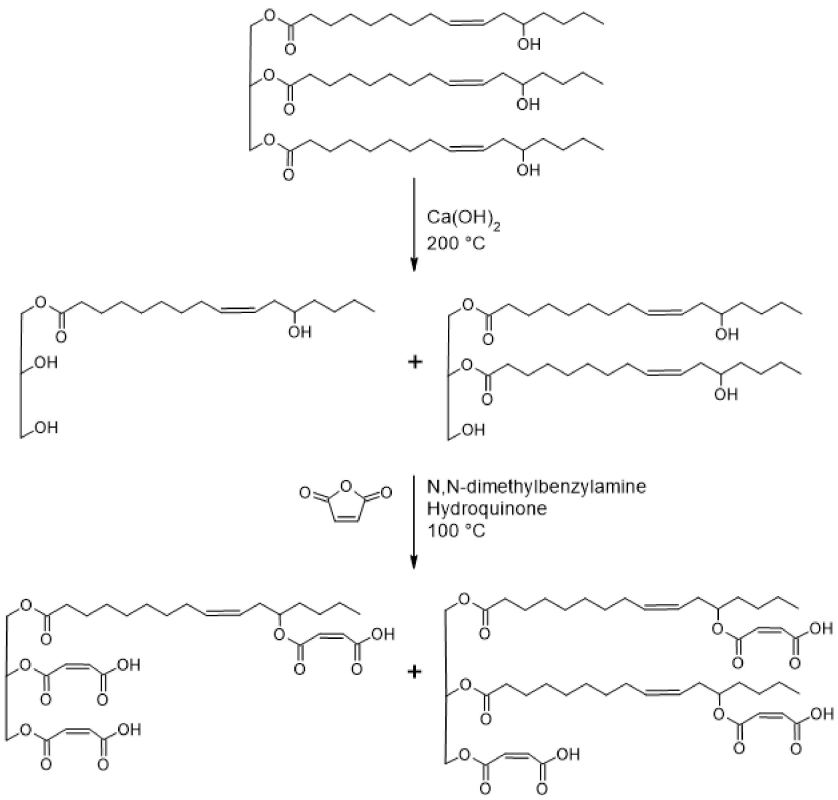

Figure 1. Schematic presentation for the synthesis of MACOG.

2.3. Preparation of Polymeric Foams

For PF1 samples, styrene (30 wt% St) was added to MACOG at 65 °C to make up a total mixture of 50.0 g and thoroughly mixed with mechanical stirring under Ar atmosphere. Surfactant (1.5 phr Ewopal 80), accelerant (0.3 phr), and initiator (3 phr BPO) were added to a 400 mL cylindrical reaction vessel. For PF2 samples, the same procedure as PF1 samples was followed, except styrene (15 wt%) and IBOMA (15 wt%) were implemented. For PF3 samples the same procedure as PF1 samples was followed, except IBOMA (50 wt%) was implemented.

Method 1: *N*,*N*-DMBA was used as the accelerant. The reaction proceeded at 75 °C with mechanical stirring for approximately 20 min. The temperature was then raised to 95 °C, after which hot water (approximately 85 °C) (4 phr) was added and the lid removed. Once the temperature increased to 95–97 °C, foaming agent (0.1–3.0 phr) was added, and the temperature increased to 100 °C as the foam rose and gelled. Curing was performed at 100 °C for 2 h in a convection oven, followed by a post-curing procedure of 120 °C for 2 h and 140 °C for 1 h.

Method 2a: *N*,*N*-DMA was used as the accelerant. The reaction proceeded for around 10 min at 65 °C until an increase in temperature was noticed due to the polymerization rate increasing. At this point $NaHCO_3$ was added and the lid removed. After about 30 s, water was added, and the foam allowed to rise and gel. Once gelled, the sample was placed in a convection oven (Universal Oven, Optolab Zone, Haryana, India) at 100 °C for 2 h, followed by a post-curing procedure of 120 °C for 2 h and 140 °C for 1 h.

Method 2b: The methodology was the same as method 2a, except the reaction was conducted at 75 °C.

The formulation and foaming method are summarized in Table 1 for each of the polymeric foam products.

Table 1. Formulation of polymeric foams.

	Styrene (wt%)	IBOMA (wt%)	$NaHCO_3$ (phr)	H_2O (phr)	Foaming Method
PF1a	30	0	1.75	4	1
PF1b	30	0	3.0	4	1
PF1c	30	0	1.5	4	2a
PF1d	30	0	2.0	4	1
PF2a	15	15	2.25	4	2b
PF2b	15	15	1.5	4	2b
PF3a	0	50	2.25	4	1
PF3b	0	50	0.1	0.5	1, 2a, 2b

2.4. Characterization Techniques

Acid value (AV) measurements were performed in accordance with ASTM D974-14e2 [29]. A sample (0.5 g) was dissolved in 50 mL of diethyl ether and ethanol mixture (50:50 v/v), or toluene and ethanol (50:50 v/v) and 1 mL of phenolphthalein indicator (1 g in 100 mL ethanol) was added to the mixture. The mixture was then titrated against 0.1 N NaOH, which was standardized against 0.1 N oxalic acid standard solution. A blank titration against the solvent mixture was performed, and this titre was subtracted from the titre containing the sample. The AV was then calculated according to Equation (1).

$$AV = \frac{56.1 \times (A - B) \times N}{G} \tag{1}$$

where A is the volume of NaOH solution consumed, B is the volume of NaOH solution consumed in a blank test, N is the normality of NaOH solution, and G the sample mass.

The saponification value (SV) was performed in accordance with ASTM D5558-95 [30]. For castor oil, COG, and MACOG, a sample (3 g) was dissolved in 50.0 mL of 0.75 N ethanolic NaOH solution. The mixture was then heated at 78 ± 2 °C under Ar atmosphere and refluxed for 1 h. Once the mixture had cooled, it was back titrated against standardized 0.5 N HCl solution. A blank measurement was performed by the aforementioned procedure without a sample. The SV was then calculated according to Equation (2).

$$SV = \frac{(A - B) \times M_{KOH} \times N_{HCl}}{m} \tag{2}$$

where A is the blank titre, B is the titre of saponified sample, M_{KOH} is the molar mass of KOH, N_{HCl} is the normality of HCl solution, and m is the mass of the sample. For both AV and SV the $Ca(OH)_2$ present in COG and MACOG was accounted for in calculations.

^{1}H nuclear magnetic resonance (^{1}H NMR) spectroscopy was performed using a Bruker Avance III 400 (400 MHz) spectrometer (Bruker, Bremen, Germany). All samples were prepared by dissolution in $CDCl_3$. Analysis was performed at 293 K with eight scans per sample, spectral width of 6009.6 Hz, and a pulse width of 10.4000 µs. The data were processed using the MestReNova software package (v. 14.2.0. Mestrelab Research, Santiago de Compostela, Spain).

A Perkin-Elmer Spectrum 100 Fourier transform infrared spectrometer using attenuated total reflection (ATR-FTIR, Waltham, MA, USA) with a universal diamond probe was used to analyze the monomer products, bulk polymers, and polymeric foams. A wavenumber range of 400–4000 cm^{-1} was collected at a resolution of 1 cm^{-1}.

The bulk polymer density (ρ_s) was measured using a pycnometer. The apparent density (ρ^*) of the polymeric foams was measured using Vernier calipers (Mitutoyo, Kawasaki, Japan) with a scale resolution of 0.02 mm and the mass was measured using an electronic an-

alytical balance with measurement to the closest 0.0001 g. The porosity (e) of the polymeric foam samples was calculated according to Equation (3).

$$e = 1 - \left(\frac{\rho*}{\rho_p}\right) \tag{3}$$

where ρ^* is the foam apparent density, ρ_p is the polymer matrix density.

The polymeric cell morphology was analyzed using a Tescan Mira3 RISE scanning electron microscope (SEM, Brno, Czech Republic). Samples were prepared into rectangles measuring 15 × 15 × 3 mm^3 and coated with Au-Pd and attached to the stage using a strip of carbon tape. Imaging was performed in secondary electron mode and an accelerating voltage of 5 kV was used with magnifications ranging between ×25 and 60. Cell diameter (D) was calculated both parallel ($D_{\parallel}$) and transverse ($D_{\vdash}$) to the foam rise. Measurements were calculated from SEM micrographs using ImageJ software package (Fiji, v. 1.52), using a minimum of 100 cells. The anisotropy ratio (R) was calculated by $D_{av\parallel}/D_{av\vdash}$ [31]. The average cell wall thickness (δ_{av}) was estimated using Aleksandrov's equation [32,33] presented in Equation (4).

$$\delta_{av} \approx D_{av}\left(\frac{1}{\sqrt{e}} - 1\right) \tag{4}$$

Polymeric foam compressive testing was performed in accordance with ASTM D1621-16 [34], with slight modifications. Compressive testing was performed on a Zwick Roell 1484 Universal Testing Machine (Ulm, Germany) with a 10 kN load cell between two flat platens, and a video extensometer was used to measure the strain. Samples (20 × 20 × 15 mm^3) were cut on a bandsaw in both parallel and transverse orientations relative to the foaming rise. Sample dimensions were measured using Vernier calipers with a scale resolution of 0.02 mm. The tests were performed at 2 mm/min to a strain of 60%. Recovery was measured after 5 min without stress after 60% strain. Compressive modulus was measured in the linear portion of the initial slope of the stress–strain graph over 1–3% strain. Compressive strength (σ_{str}) was measured at 10% strain. Collapse stress (σ_{col}) was measured as the first point on the stress–strain graph where $\frac{d\sigma}{d\varepsilon} = 0$, or as a tangent to the plateau. The proportional limit (σ_{prop}) was measured as the greatest stress where there was proportionality of stress-to-strain (Hookean behavior), measured at the point where the slope of the graph was still >96% of the modulus. The plateau stress (σ_{plat}) was measured at 20% strain. The strain at the onset of densification (ε_{OD}) was measured by calculating the absorbed energy efficiency (W_E) according to Equation (5), whereby ε_{OD} was calculated at the peak of the graph according to Equation (6). The energy absorbed until onset of densification (W_{OD}) was measured according to Equation (7), using the ε_{OD} value measured from Equation (6). [35,36]. W_{tot} was calculated using the same equation, but changing the upper limit to 60%. σ_{plat}, ε_D, and W were calculated using MathWorks MatLab (V. R2020a) by applying a cumulative trapezoidal numerical integration method.

$$W_E = \frac{1}{\sigma(\varepsilon)} \int_{\varepsilon_y}^{\varepsilon} \sigma(\varepsilon) d\varepsilon \tag{5}$$

$$\frac{d\eta(\varepsilon)}{d\varepsilon}|_{\varepsilon=\epsilon_{OD}} = 0 \tag{6}$$

$$W_{OD} = \int_0^{\varepsilon_{OD}} \sigma(\varepsilon) d\varepsilon \tag{7}$$

2.5. Biodegradability of Polymeric Foams

Initially, the polymeric samples (20 × 10 × 10 mm^3) were cleaned using compressed air to remove any loose particles present from sectioning. Samples were then placed under various biodegradation conditions: (1) An aerobic laboratory soil burial with soil composition similar to that described in ASTM D5988 [37]; (2) a comparative aerobic soil burial in a "natural" environment buried 50 mm in an established compost-rich garden

during an austral summer. The relative mass loss was established by periodically removing the samples (removing as much debris as possible with low pressure compressed air) and measuring the mass loss compared to the initial sample mass according to Equation (8).

$$Mass\ loss = \frac{m_0 - m_i}{m_0} \times 100 \quad (8)$$

where m_0 is the initial mass and m_i is the mass at a given time.

The laboratory control samples were kept in 5 L buckets at ambient temperature, each containing 1 polymeric foam sample and 1 polyurethane (PU) negative control sample, which were sealed with a lid with a small hole (1-mm diameter) to avoid potential CO_2 gas build-up. The buckets were opened once per week for 15 min to replenish oxygen content. Additionally, the soil was lightly turned monthly while the samples were removed for measurements.

2.6. Statistical Analysis

Cell diameter log-normal distribution plots were performed using XLSTAT (Addinsoft, v. 2020.5, Long Island, NY, USA) in Excel 2010. For biodegradation, a Shapiro test for normal distribution was performed, where all data were normally distributed except for month two laboratory environment. Therefore, an unpaired student's *t*-test was performed for month 1 data and an unpaired two-samples Wilcoxon test for other data. Statistically significant factors were established for *p*-values at a 95% confidence level ($p < 0.005$). All graphs indicate the mean ± standard error of the mean. *AV* and *SV* measurements were an average of three samples. All mechanical and biodegradation results were an average of five samples.

3. Results and Discussion

3.1. Synthesis of Castor Oil Glycerides and Maleated Castor Oil Glycerides

The base-catalyzed glycerolysis of castor oil was successfully performed to produce COG. The product was characterized by ^{1}H NMR (see Supplementary Materials Figure S1a) and ATR-FTIR (see Supplementary Materials Figure S2), with the characteristic ATR-FTIR peak assignments summarized in Table S1 of the Supplementary Materials. The COG produced was then successfully maleated through esterification of the hydroxyl groups with maleic anhydride to produce MACOG. The product was characterized by ^{1}H NMR (see Supplementary Materials Figure S1b) and ATR-FTIR (see Supplementary Materials Figure S2), with the characteristic ATR-FTIR peak assignments summarized in Table S1 of the Supplementary Materials. The MACOG product was used directly in the preparation of polymeric foams, without purification.

3.2. Preparation of Polymeric Foams

Thermosetting polymer foams usually need reactive foaming, as the polymer cannot be foamed post-polymerization in the way most thermoplastic polymeric foams are processed [38]. The temperature-temporal relationship between polymer gelling and foaming is therefore critical to ensure optimal foam morphology as well as a high degree of curing. As a result, a delayed addition of foaming agent methodology was implemented. A similar delayed addition of foaming agent has previously been employed by various other groups with improved morphology and properties reported [39–41]. The foaming/curing process was not straightforward, and considerable effort was made to optimize and refine the foaming/curing process to achieve polymeric foams with consistent morphology and optimized properties. Two general approaches were taken for the delayed addition of the foaming agent: either to increase the temperature progressively until adding the foaming agent prior to a known temperature of rapid cure was met (method 1), or to maintain a constant temperature for a fixed period until adding the foaming agent when the polymerization reaction increased in rate (method 2). It was found that too early addition of foaming agent could lead to coarsening of the cellular structure as depicted in Figure 2a, or total foam

collapse. Conversely, too late addition of foaming agent could lead to cracking as gelling occurred while the foam was still rising, as depicted in Figure 2b. It was thus found that a short window in between these two events could be exploited to achieve an optimized, consistent cell morphology, as depicted in Figure 2c,d. Additionally, it was necessary to employ N,N-DMA as an accelerant when IBOMA was incorporated to maintain practical foam preparation temperatures.

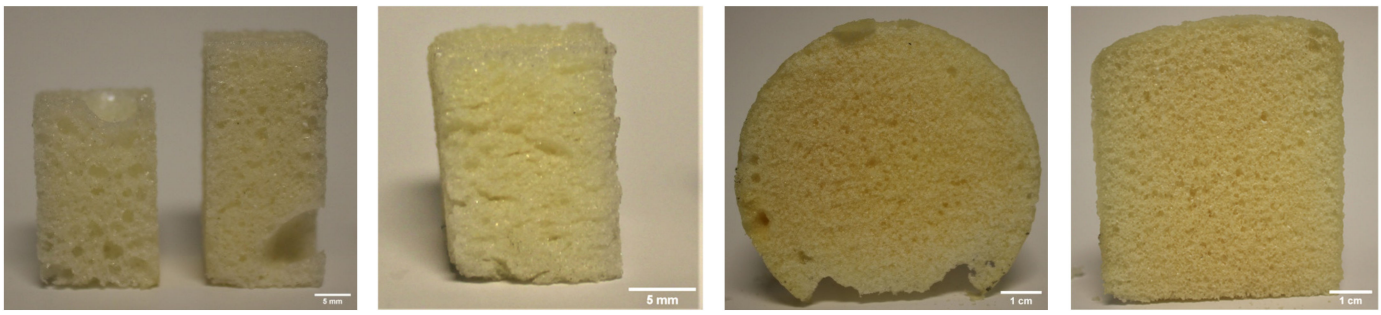

(**a**) (**b**) (**c**) (**d**)

Figure 2. Polymeric foam product with (**a**) coarsening due to early addition of foaming agent, (**b**) cracking due to too late addition of foaming agent, (**c**,**d**) optimized addition of foaming agent.

For PF3, several of the methods (methods 1, 2a, 2b) were explored to try successfully preparing polymeric foams. It was found that although stable foams could be formed in the reactive mixture, once cured the polymeric foams lacked any structural integrity and could be readily crumbled. One hypothesis for this effect was that the ester bonds present on IBOMA were highly susceptible to hydrolysis, such that introducing water at elevated temperature to induce foaming caused scission of the monomer. However, waterborne polymerization at 70 °C incorporating IBOMA has been demonstrated without reported hydrolysis, which disputed this hypothesis [42]. It was further speculated that the presence of acid groups on MACOG may have catalyzed the hydrolysis. However, it is also known that methacrylic esters are less susceptible to hydrolysis in both acidic and alkaline environments than acrylic acid esters [43]. In an attempt to minimize the suspected hydrolysis side reaction, a minimum of foaming agent and water were employed (0.15 phr $NaHCO_3$ and 0.5 phr H_2O). However, the polymeric foam still lacked structural integrity and could be easily crumbled. Another hypothesis was that there could have been dissolved oxygen in the water, causing retardation of the polymerization or the formation of low molecular weight polymers. Extensive curing of the polymeric foam at 100 °C for >48 h did not appreciably change the structural integrity of the product though. While the mechanism causing this effect remained unknown, it was concluded that this method of foaming was not suitable to produce PF3.

3.3. Polymeric Foam Cell Morphology

The apparent density (ρ^*), porosity (e), average cell diameter (D_{av}), and average cell wall thickness (δ_{av}) were measured for PF1 and PF2 samples both parallel and perpendicular to foam rise direction, as summarized in Table 2. SEM micrographs and corresponding cell diameter distributions are presented in Figure 3.

Table 2. Polymeric foam cell morphology.

	ρ^* (g/cm^3)	e	$D_{av\parallel}$ (μm)	$D_{av\perp}$ (μm)	R	$\delta_{av\parallel}$ (μm)	$\delta_{av\perp}$ (μm)
PF1a	0.189 ± 0.003	0.83	612 ± 24	417 ± 16	1.47	60	41
PF1b	0.125 ± 0.006	0.89	709 ± 34	551 ± 29	1.29	43	33
PF1c	0.241 ± 0.007	0.78	409 ± 21	274 ± 12	1.49	54	36
PF1d	0.168 ± 0.004	0.85	222 ± 8	192 ± 7	1.16	19	16
PF2a	0.168 ± 0.004	0.85	410 ± 17	384 ± 19	1.07	35	33
PF2b	0.309 ± 0.008	0.73	246 ± 11	195 ± 7	1.26	42	33

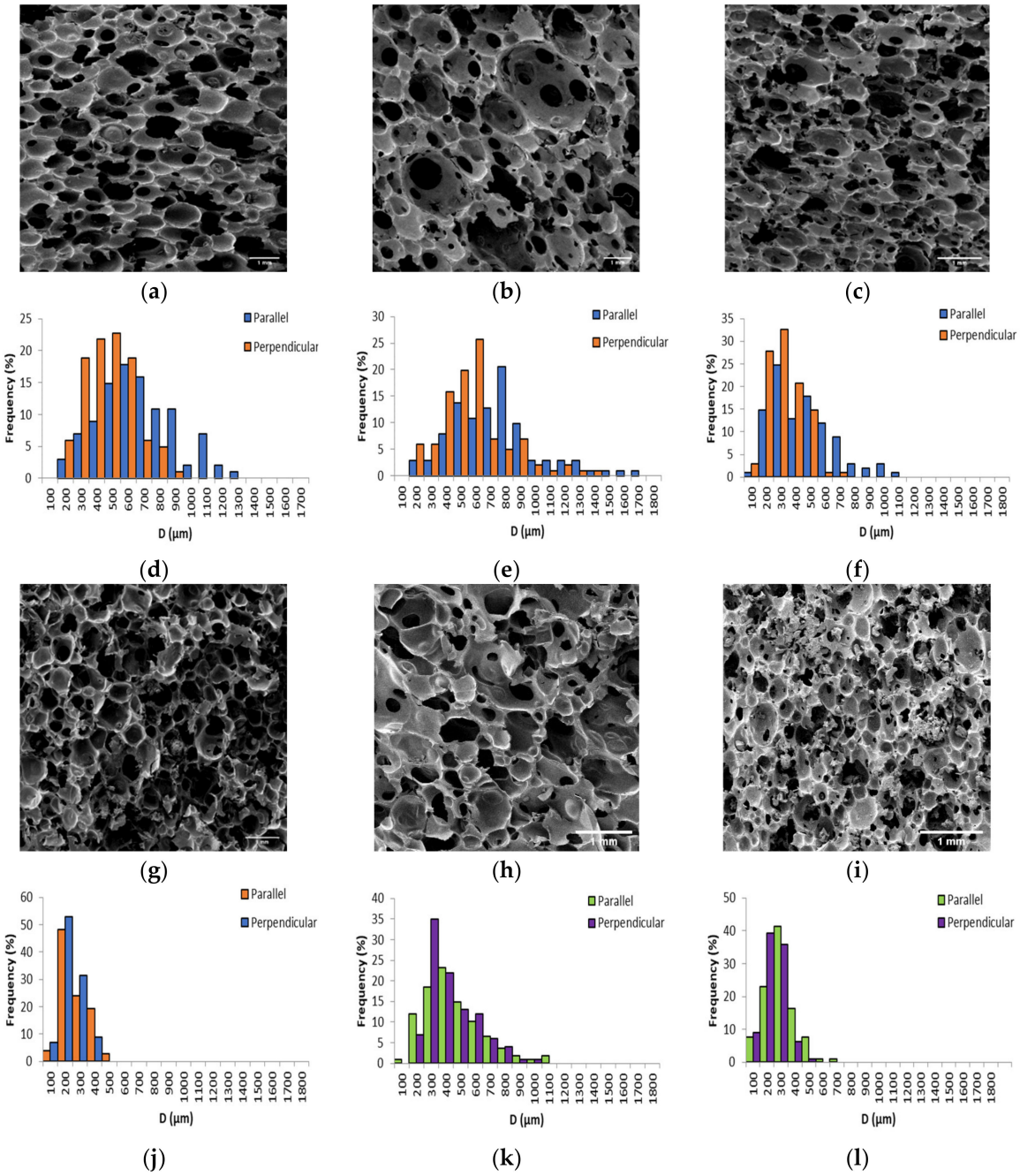

Figure 3. (**a**–**c**) SEM micrograph of PF1a, PF1b, and PF1c, (**d**–**f**) cell diameter distribution of PF1a, PF1b, and PF1c, (**g**–**i**) SEM micrograph of PF1d, PF2a, and PF2b, and (**j**–**l**) cell diameter distribution of PF1d, PF2a, and PF2b.

The ρ^* of the PFs ranged between 0.126 ± 0.005 g/cm^3 and 0.309 ± 0.008 g/cm^3, placing them in the range of medium to high density polymeric foams. This demonstrated that a wide range of ρ^* could be tailored by altering the amount of foaming agent employed. Furthermore, the ρ^* achieved were in a similar range to many other VO-derived polymeric foams [13,14,17,22,23,44,45]. The *e* ranged between 0.78 and 0.89, which was comparable or higher than that achieved for similar VO-derived polymeric foams [41,44,46,47]. Since it is well-known that the cell morphology of PFs is often anisotropic when allowed to foam freely in one direction, the average cell diameter (D_{av}) parallel and perpendicular to the foam rise were measured [48].

The D_{av} as a function of ρ^* was plotted in Figure 4. With the exceptions of PF1d and PF2a (both ρ^* 0.168 g/cm^3) a general decrease in D_{av} with increasing ρ^* was observed for both parallel and perpendicular measurements. However, R values displayed no obvious dependence on ρ^*. A particularly good example of such was for PF1d and PF2a, which had the same ρ^* but displayed very different R. This difference could have been due to a difference in processing conditions or curing kinetics. However, for PF1 samples, where processing conditions and curing kinetics were kept as similar as possible, there was still a fluctuation in R seemingly independent of ρ^*.

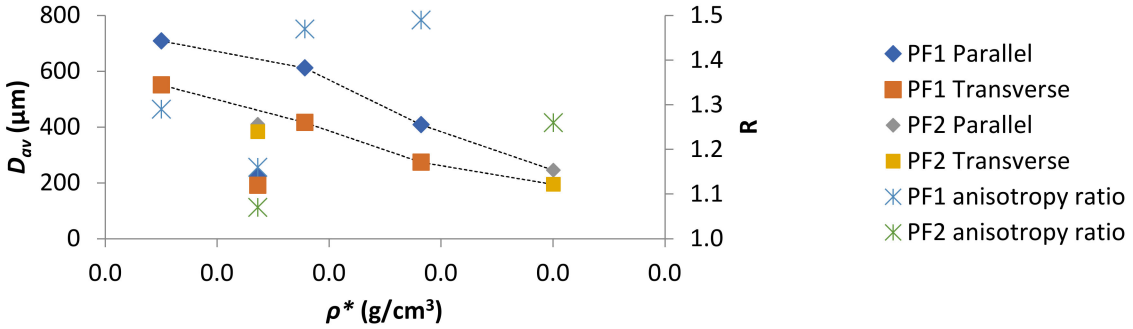

Figure 4. PF D_{av} and R as a function of ρ^*.

The distribution of cell diameters has most commonly been modeled to a log-normal distribution [46,49–54]. The results for PF1 and PF2 fit a log-normal distribution, right-skewed toward larger cell diameters, as plotted in Figure 5a,b for the parallel and perpendicular directions, respectively. The variance of the distributions was plotted as a function of D_{av} in Figure 5c. It was apparent that distributions were generally wider for larger D_{av}, which was in agreement with other literature [55].

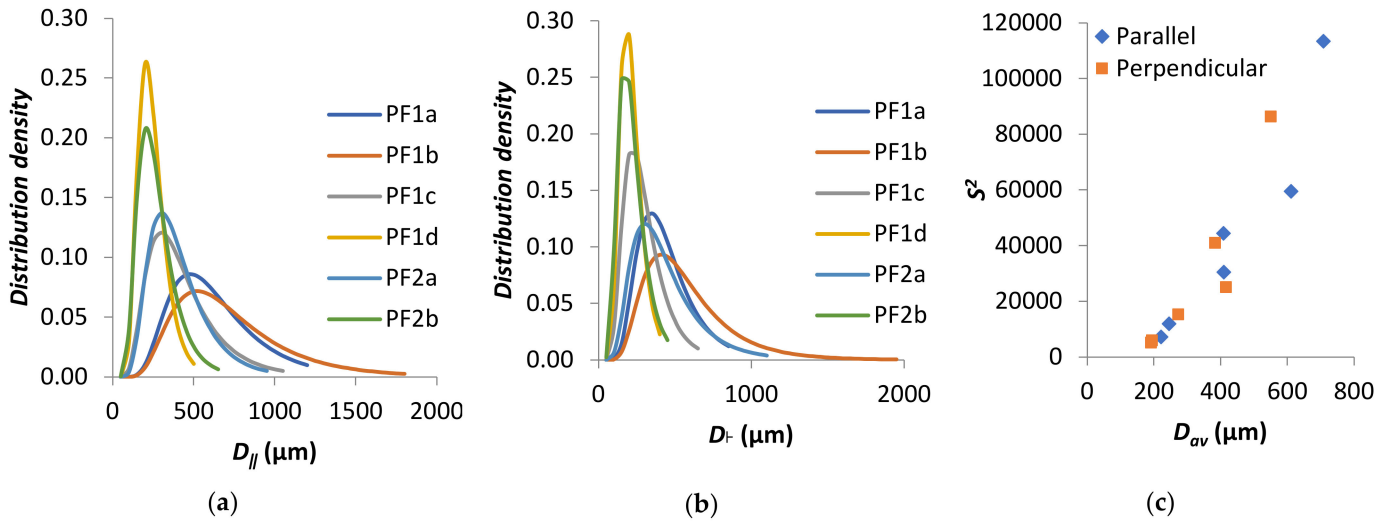

Figure 5. Log-normal density distribution for PF1 and PF2 samples in (**a**) parallel direction and (**b**) perpendicular direction. (**c**) S^2 as a function of D_{av}.

3.4. Compressive Properties

The uniaxial compressive properties of PF1 and PF2 samples were analyzed, with samples compressed parallel to the foam rise (ParFR) direction plotted in Figure 6a,b, respectively. Furthermore, the compressive properties of samples PF1a and PF1b were compressed perpendicular to the foam rise (PerFR). The characteristic compressive properties for the PFs are summarized in Table 3. The compressive properties were measured for both ParFR and PerFR because it was anticipated that the anisotropic cell morphology would result in anisotropic compressive properties [56].

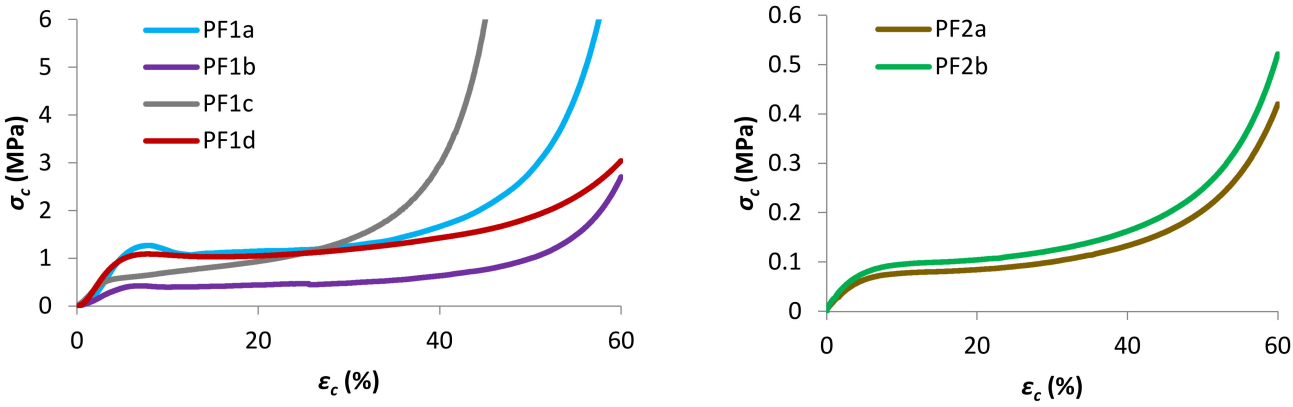

(**a**) (**b**)

Figure 6. Representative compressive σ_c–ε_c plots (**a**) PF1 ParFR and (**b**) PF2.

Table 3. Compressive properties of PF1 and PF2.

	E_c (MPa)	σ_{prop} (MPa)	σ_{col} (MPa)	σ_{str} (MPa)	σ_{plat} (MPa)	Recovery (%)
PF1a ParFR	26.85 ± 1.07	0.70 ± 0.069	1.15 ± 0.066	1.11 ± 0.021	1.79 ± 0.172	54 ± 1.6
PF1a PerFR	15.69 ± 0.65	0.38 ± 0.023	0.57 ± 0.014	0.64 ± 0.033	0.80 ± 0.033	65 ± 1.7
PF1b ParFR	8.37 ± 0.46	0.25 ± 0.023	0.40 ± 0.015	0.39 ± 0.019	1.25 ± 0.33	60 ± 1.9
PF1b PerFR	3.51 ± 0.43	0.11 ± 0.0079	0.18 ± 0.019	0.19 ± 0.017	0.20 ± 0.017	86 ± 1.0
PF1c	23.31 ± 1.49	0.57 ± 0.011	1.00 ± 0.038	1.01 ± 0.044	1.05 ± 0.064	81 ± 1.0
PF1d	20.13 ± 1.73	0.57 ± 0.14	0.73 ± 0.12	0.79 ± 0.0761	1.01 ± 0.090	56 ± 1.0
PF2a	1.13 ± 0.107	0.048 ± 0.0033	0.072 ± 0.010	0.075 ± 0.0053	0.083 ± 0.0066	79 ± 1.0
PF2b	1.38 ± 0.055	0.057 ± 0.0039	0.085 ± 0.0030	0.088 ± 0.0031	0.092 ± 0.0031	71 ± 0.9

PF1c was prepared using method 2b, as opposed to method 1 that was used for PF1a, b and d. It was apparent that the processing conditions could have affected the overall mechanical properties of the polymeric foams, as in most cases PF1c did not match the relationships that correlated well between PF1a, b, and d. It was for this reason that PF1c was excluded from the relationships in most cases. This phenomenon was considered interesting and therefore the result has been reported, but more PF1 samples would need to be prepared using method 2b to verify that it was the processing conditions that caused the observed discrepancy.

Generally, the compressive properties of the polymeric foams displayed three distinct stages on a σ_c–ε_c graph: an elastic stage, a plateau stage, and a densification stage. An initial linear elastic region was seen on the σ_c–ε_c graphs, observed at low strains (ε_c < 5%) for all polymeric foams. This region corresponded to the bending of cell edges and struts, cell membranes stretching (for closed cells) and to a lesser extent gas pressure within closed cells [38,56].

The Young's modulus (E_c) was calculated in this region of the graph, between ε_c of 1–3%. The E_c as a function of ρ^* was plotted in Figure 7 for PF1 ParFR and PF1 PerFR. It was evident that E_c increased with increasing ρ^* in both ParFR and PerFR; with a maximum E_c

of 26.85 ± 1.07 MPa for PF1a ParFR using styrene as reactive diluent, and 1.38 ± 0.055 MPa for PF2b using styrene and IBOMA as reactive diluent. It has previously been established that there is a power–law relationship between E_c and ρ^*, according to Equation (9).

$$E_c = B\rho^{*m} \tag{9}$$

where ρ^* is the apparent density of the PF, B is a constant related to the physical properties of the resin, and m is a density exponent related to the structure and deformation mechanics of the PF.

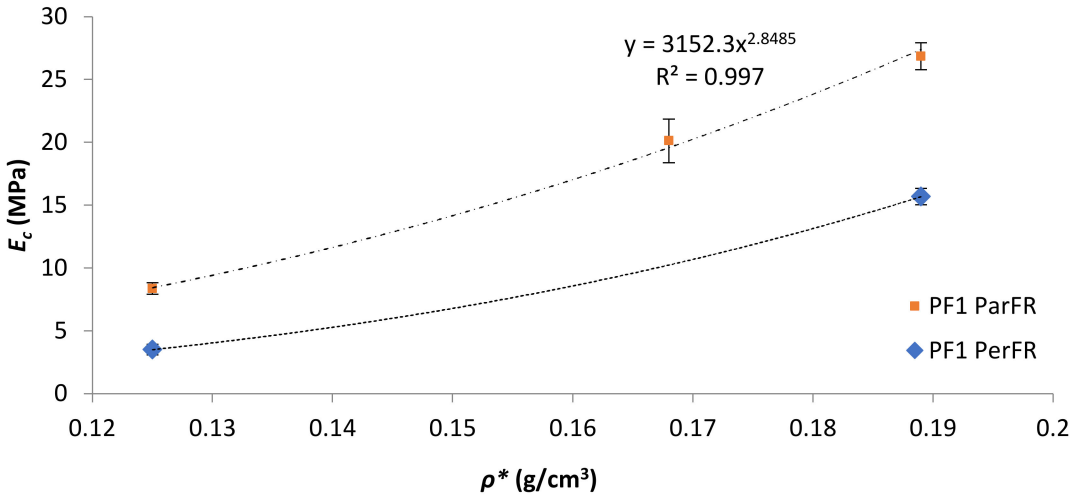

Figure 7. E_c as a function of ρ^* for PF1.

PF1 ParFR fit a power–law relationship (R^2 = 0.9984) with a B value of 3152 MPa and an m value of 2.85. Wang et al. [22] calculated a B value of 514 MPa and an m value of 3.55 for MACO/St (30 wt% St) polymeric foams. Furthermore, it was reported that both B and m values increased with increasing St wt% (10–40 wt% reported) due to the rigid contributions of the stiff, aromatic reactive diluent. Based on the model, the larger B value reported here suggested it was the polymer matrix properties that contributed to the superior results of that of the MACO/St polymeric foams [57]. PF2 E_c displayed a far weaker dependence on ρ^*, whereby almost doubling ρ^* between PF2a (1.13 ± 0.11 MPa) and PF2b (1.38 ± 0.06 MPa) resulted in a marginal increase in E_c. This could have been due to fundamental differences in cell morphology between the samples [58].

It was apparent that there was a large difference in $E_{c\|}$ and $E_{c\vdash}$ observed for PF1a and PF1b, as visualized in Figure 7. The difference in $E_{c\|}$ relative to $E_{c\vdash}$ has been reported to be partially influenced by differing deformation mechanisms in anisotropic polymeric foams; whereby parallel to the foam rise there is axial deformation of the cell edges oriented parallel to the loading axis, while perpendicular deformation is carried by axial loading and bending of the cell edges and is hence dependent on the cell edges' stiffness. This implies that a stiff linear response was seen until cell instability (beyond σ_{prop}) in parallel, which was not the case for perpendicular, where stress due to cell edges bending increases to a lesser degree with progressive ε_c [59]. Gibson and Ashby [48] developed a model that proposed a direct proportionality between R and $E_{\|c}$, such that $E_{\|c}$ increased with increasing R, since at greater R the walls are relatively longer in the parallel direction. The specific $E_{\|c}$ of PF1a ParFR (0.142 ± 0.006 MPa·m^3/kg) was higher than PF1b ParFR (0.067 ± 0.004 MPa·m^3/kg) and $R_{PF1a} > R_{Pf1b}$, which was in agreement with this model and other literature [31,55,60]. The proportional limit (σ_{prop}) was measured as the σ_c at which deviation from Hookean behavior relative to ε_c was observed, thus at the onset of plastic compressive behavior. The σ_{prop} as a function of ρ^* was plotted in Figure 8a; and it was evident there was a correlation with increasing σ_{prop} and increasing ρ^*.

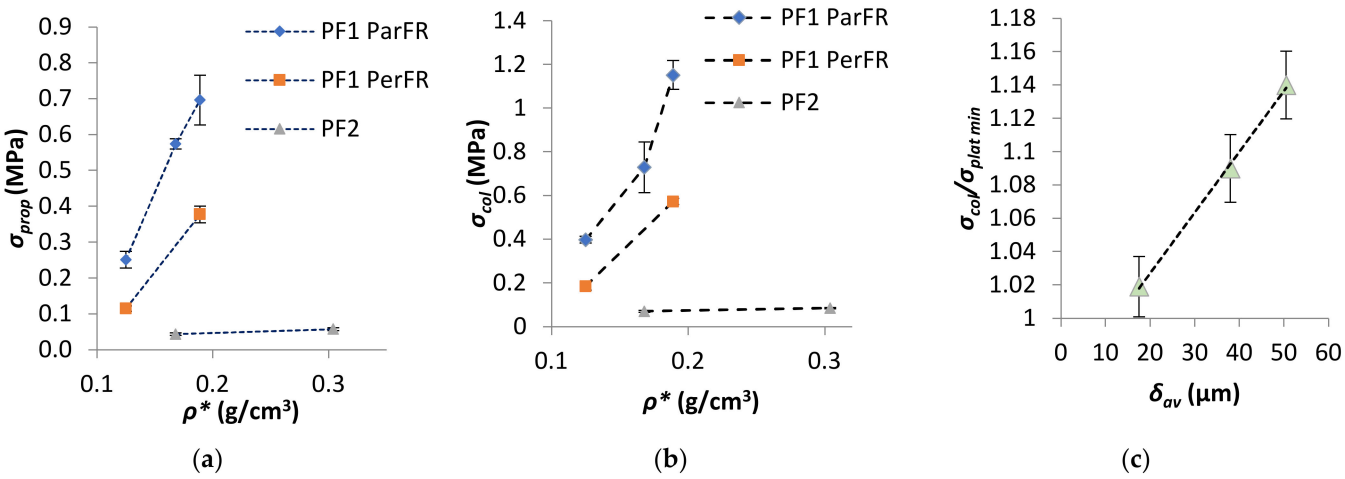

Figure 8. (**a**) σ_{prop} as a function of ρ^* for PF1, (**b**) σ_{col} as a function of ρ^*, and (**c**) ratio of $\sigma_{col}/\sigma_{plat\ \min}$ as a function of δ_{av} for PF1 ParFR.

The collapse stress (σ_{col}) was measured at the local peak of the σ_c–ε_c graph after σ_{prop} for PF1 ParFR and as a tangent to the plateau for PF1 PerFR and PF2. The σ_{col} as a function of ρ^* was plotted in Figure 8b where it was apparent that there was a correlation between increasing σ_{col} and increasing ρ^*. Furthermore, it appeared that there were two dominant modes of collapse stress: elastic buckling (PF1 PerFR, PF1c ParFR, PF2) and plastic collapse (PF1a, b, d ParFR) [48,61]. This was observed by a region of strain-softening evident for PF1 ParFR (except PF1c), which was not observed for PF1 PerFR and PF2. For PF1 this could have been due to a difference in deformation mechanisms due to cell anisotropy. It has been reported that cell elongation parallel to the compression axis favors plastic collapse, whereby if the fully plastic moment of the cell edge is exceeded, plastic hinging at the strut occurs. On the other hand, cell elongation perpendicular to the compression axis favors elastic buckling, whereby if the Euler load on the cell edge is exceeded buckling occurs, which is proportional to the edges' flexural stiffness [31]. As a result, when extensive plastic collapse occurred for PF1 ParFR a decrease in the PFs ability to retain load bearing capacity was observed [48,62]. The extent of strain softening has previously been demonstrated to correlate well with ρ* by Lee et al. [63] and Lim et al. [62]. However, this was not evident for PF1 samples; rather, it was found that the extent of strain softening, measured by the ratio of $\sigma_y/\sigma_{plat\ min}$, correlated to the δ_{av}, as plotted in Figure 8c. Although there is often a relationship between ρ^* and δ_{av}, this is not always the case, as was demonstrated for PF1d and PF2a, which displayed similar density but very different δ_{av}. During compression, $\delta_{av\parallel}$ was related to those undergoing axial loading during plastic collapse, while $\delta_{av\vdash}$ was related to bending of those perpendicular to compression axis, thus δ_{av} was used in calculation [31,48,59]. PF1c and PF2 did not display strain softening, despite being anisotropic. This could be due to a fundamental difference in polymerization/processing, causing the PFs to respond in a typical elastomeric manner instead of elastoplastically [38]. It was worth noting that while PF2 contained a different polymer matrix to PF1c, both PF2 and PF1c were prepared by method 2a/b as opposed to method 1 for PF1a, b and d.

At ε_c beyond the point of σ_{col} and strain softening (if apparent), the polymeric foams displayed a plateau stage. During the plateau stage, deformation and stress response were accounted for by cells collapsing via elastic and/or plastic buckling mechanisms, walls and edges being ruptured throughout the material and gas pressure in closed cells. Typical to the plateau stage, low changes in σ_c over a large ε_c range were observed for the polymeric foams, although the plateau moduli were positive in all polymeric foams. One contributing factor to the positive plateau modulus could have been gas pressure within closed cells [38]. In the plateau region deformation can occur through elastomeric, elastoplastic, and brittle modes. For elastomeric deformation, no plastic deformation occurs to cell edges, struts, and walls, and deformation is accounted by a pure elastic

buckling mechanism. For elastoplastic deformation there is plastic deformation of the cell edges, struts, and walls. These phenomena are observed differently within the cellular structure; elastomeric response is characterized by uniform distribution of deformation, while elastoplastic is characterized by progressive local deformation of the cell layers acting as "deformation fronts" of the weakest cell layer [56]. It is common for a combination of modes to be present in a polymeric foam. Brittle failure was not observed as the dominant mode during the plateau region for all polymeric foam, which is typically characterized by a jagged σ-ε plot [38]. This suggested that the fatty acid chains on MACOG provided mobility to the polymer.

The σ_{str}, measured at ε_c of 10% for semi-rigid and rigid polymeric foam, was within the plateau stage for all polymeric foams. It was apparent that σ_{str} increased with increasing ρ^*; with a maximum σ_{str} of 1.11 ± 0.021 MPa for PF1a ParFR using styrene as the reactive diluent, and 0.088 ± 0.0031 MPa for PF2b using styrene and IBOMA as reactive diluent. There was a power–law relationship between σ_{str} and ρ^* according to Equation (10). This relationship was plotted in Figure 9a for PF1, where a power–law relationship (R^2 = 0.9985) was fit with an A value of 71 MPa and n value of 2.5 for PF1 ParFR.

$$\sigma_{str} = A\rho^{*n} \tag{10}$$

where ρ^* is the apparent density of the PF, A is a constant related to the physical properties of the resin, and n is a density exponent related to the structure and deformation mechanics of the PF.

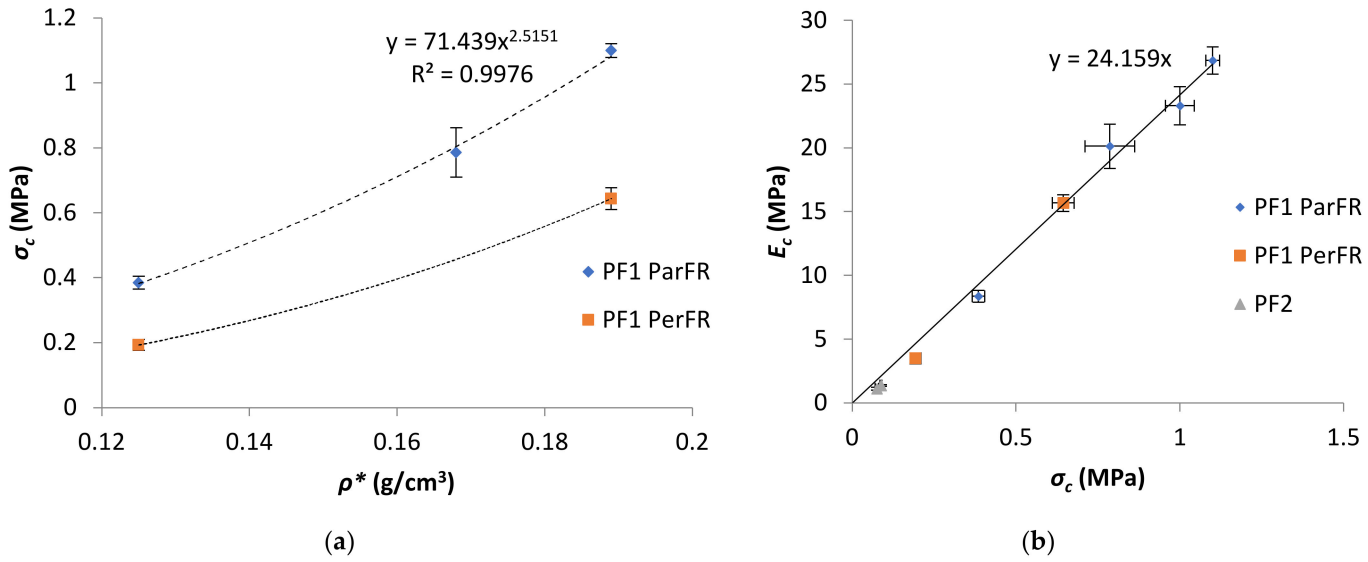

Figure 9. (**a**) σ_c as a function of ρ^* for PF1 and (**b**) E_c as a function of σ_c.

According to Gibson and Sanders [64] a theoretical n value of 2 relates to closed cell polymeric foams, while n values of 1.5 and 1.36 relate to open cell and hollow sphere cell polymeric foams, respectively, and fit well with previous experimental literature [12,57,65–67]. However, it was also evident from literature that deviation from the theoretical model with $n < 2$ was not unusual for polymeric foams [22,67]. The n value for PF1 ParFR was in agreement with the cellular deviation from spheres associated with porosities greater than 0.63 and majority closed cell content [68].

A linear correlation between σ_{str} and E_c was established for PF1 ParFR (R^2 = 0.985), as plotted in Figure 9a, with a slope of 24.2. A linear relationship has also been reported by Bonaillie [12] for AESO polymeric foams with a slope of 17. The larger slope here indicated a greater relative elastic stiffness, which could be partially attributed to the anisotropy of cells and introduction of hard segments from the reactive diluent compounds. Although the compressive moduli and strength of PF2 were substantially lower than those of PF1,

these results were still higher than other polymeric foams reported in literature that were produced with a greater weight percentage of styrene. For example, PF2a displayed a σ_{str} (87.6 ± 3.1 kPa) more than double that of MACO/St (20 wt% St) PF (33.8 ± 1.2 kPa) of similar ρ^* produced by Wang et al. [22]. Furthermore, PF2 displayed compressive properties that were comparable to various other bio-based semi-rigid PFs [23,69,70]. However, it was also possible that the issues associated with preparing PF3 could also have contributed to the lower mechanical properties in PF2.

Lastly on the σ_c–ε_c plot, densification occurred once the cell walls completely collapsed, causing compaction against each other and the material began acting as a homogeneous solid. Densification was denoted by a steep rise in σ_c over a small ε_c [56]. The differentiation between the terms "densification strain" (ε_D) and "onset of densification strain" (ε_{OD}) has often remained ambiguous or been used interchangeably. However, these two measurements are distinct, whereby the ε_{OD} occurs when the deformation modes typical of the plateau region are suppressed due to contact between the cell walls and edges, and precedes the ε_D; whereas ε_D is the point where the polymeric foam is completely compacted [35,71]. From a product design application perspective, the ε_{OD} is a more useful parameter to consider, as it can be used to calculate the energy the polymeric foam is able to absorb before it acts as a homogenous solid [44]. The ε_{OD} was calculated by implementing the methodology of Tan et al. [36], which was further developed for polymeric cellular solids by Li et al. [35] as a reliable method within literature [40,71–75]. The energy absorption characteristics have been summarized in Table 4.

Table 4. Energy absorption properties.

	Orientation	ε_{OD} (%)	$W_{E\ at\ OD}$ (%)	W_{OD} (J/cm^3)	W_{tot} (J/cm^3)
PF1a	ParFR	38.0 ± 0.364	27.41 ± 0.16	40.22 ± 1.85	124.4 ± 7.93
	PerFR	29.01 ± 0.63	17.77 ± 0.21	20.39 ± 0.96	120.02 ± 1.77
PF1b	ParFR	41.9 ± 0.83	27.35 ± 1.76	18.36 ± 1.68	41.17 ± 5.43
	PerFR	53.28 ± 0.78	33.29 ± 0.71	11.82 ± 0.90	14.61 ± 1.32
PF1c	ParFR	49.16 ± 0.53	30.48 ± 0.63	56.02 ± 2.52	81.53 ± 4.27
PF1d	ParFR	31.86 ± 1.92	17.45 ± 0.34	29.69 ± 1.24	134.66 ± 1.98
PF2a	ParFR	48.97 ± 0.99	27.31 ± 0.43	4.53 ± 0.312	8.22 ± 0.28
PF2b	ParFR	44.69 ± 0.49	25.35 ± 0.64	4.18 ± 0.20	8.18 ± 0.58

Strain at onset of densification (ε_{OD}) and energy absorption efficiency at onset of densification ($W_{E\ at\ OD}$) both increased with increasing D_{av} in all cases, as plotted in Figure 10a,b, respectively. The results of ε_{OD} increase with D_{av}, as in agreement with the literature [76]. Furthermore, it was apparent that both the ε_{OD} and $W_{E\ at\ OD}$ were higher for PF2 than PF1 ParFR.

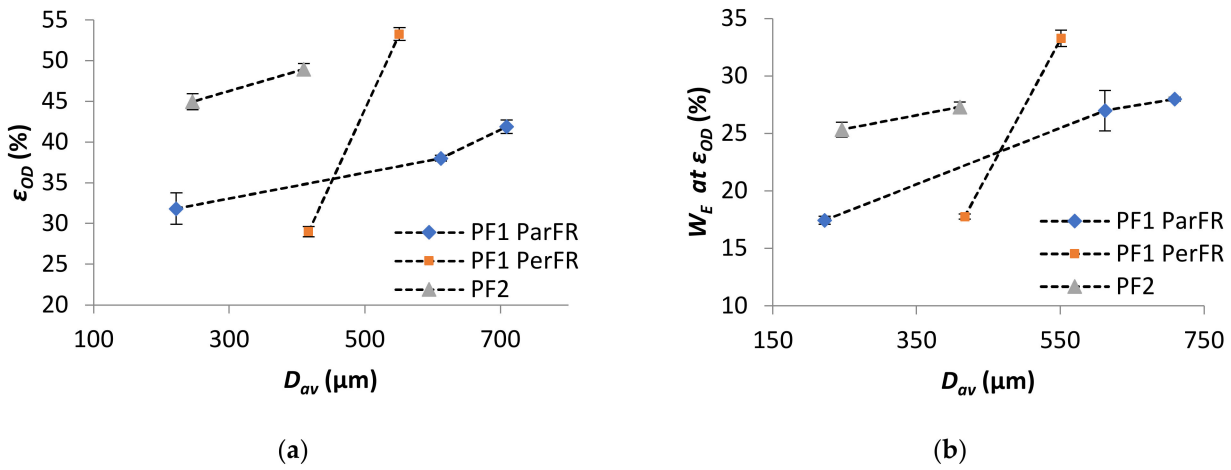

Figure 10. (**a**) ε_{OD} as a function of D_{av} and (**b**) W_E as a function of D_{av}.

The energy absorbed at the onset of densification (W_{OD}) increased with increasing ρ^* in all cases, as plotted in Figure 11. The comparative W_{OD} for PF1b ParFR and PF1b PerFR was similar, while PF1a ParFR was higher than PF1a PerFR. This was particularly interesting, as both the $W_{E\ at\ OD}$ and ε_{OD} were lower for PF1a PerFR than PF1b PerFR. This result could have arisen due to the differing deformation modes during the plateau region, since PF1a displayed a larger anisotropy than PF1b. Furthermore, the W_{OD} was higher for PF1 than PF2, even though both W_E and ε_{OD} were higher for PF2 than PF1. This result suggested that while PF2 was able to absorb energy at both a higher efficiency and until greater strains, the energy absorption was still limited by the properties of the polymer matrix. Furthermore, the deformation modes described during the plateau stage were thought to be similar to that of PF1 PerFR as previously described, which could have further contributed to this result.

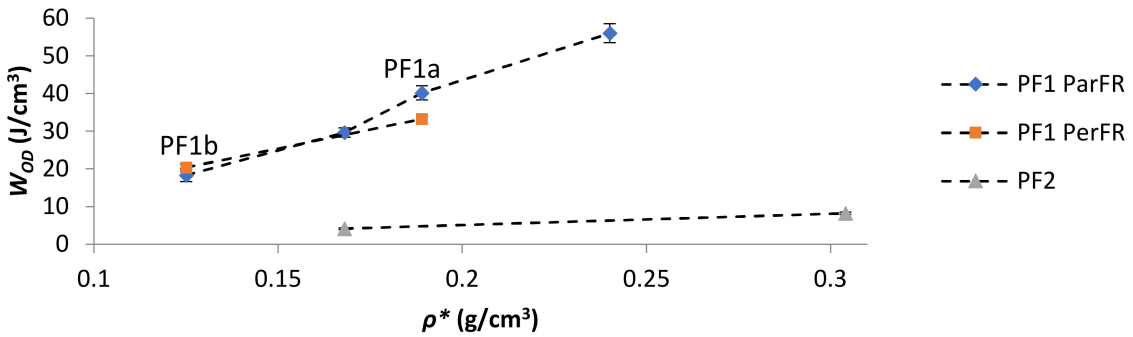

Figure 11. W_{OD} as a function of ρ^*.

W_E as a function of σ_c was plotted in Figure 12a for PF1 ParFR, Figure 12b for PF1 PerFR, and Figure 12c for PF2. There was linear proportionality between W_E and σ_c until the σ_{prop}. Following the proportional limit, W_E increased rapidly, with a maximum close to σ_{col}. W_E slowly decreased until the σ_c at ε_{OD}, and then continued to decrease progressively at σ_c beyond ε_{OD}. A similar relationship between W_E and these characteristic σ values has been reported in literature [74,75,77,78].

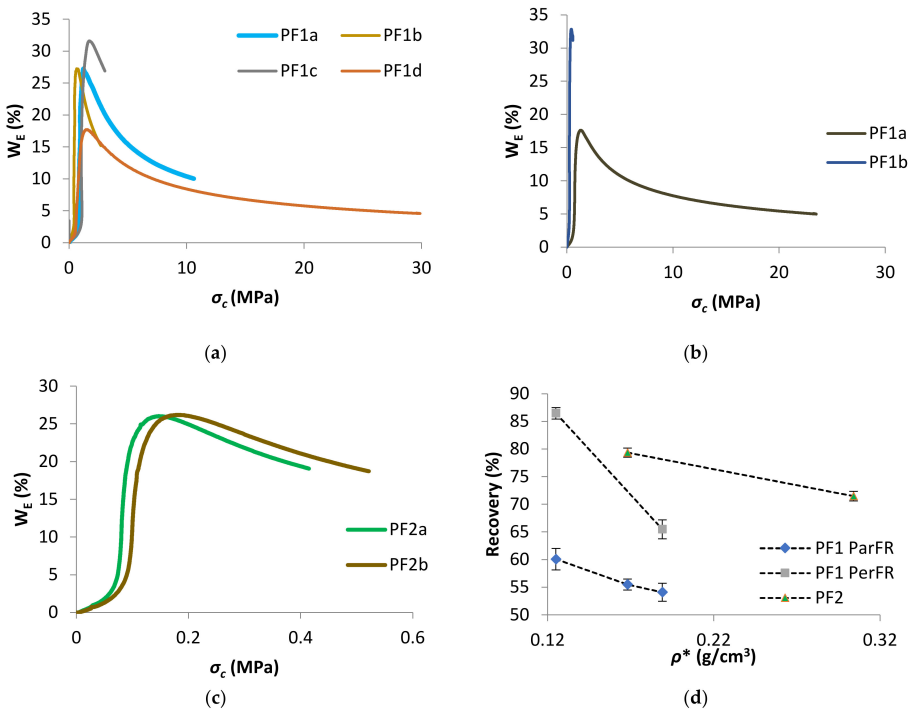

Figure 12. W_E as a function of σ_c for (**a**) PF1 ParFR, (**b**) PF1 PerFR, and (**c**) PF2, and (**d**) recovery as a function of ρ^* for PF1 ParFR, PF1 PerFR and PF2.

The recovery as a function of ρ^* was plotted in Figure 12d, which showed increasing ρ^* correlated with decreasing recovery for all polymeric foams. It was possible that the higher recovery displayed by PF1 PerFR was due to dominant elastomeric deformation during the plateau stage, compared to elastoplastic deformation in PF1 ParFR. When stress was removed elastomeric contributions had a greater ability to return to original geometry, while elastoplastic deformation cannot. Likewise, PF2 recovery were higher than PF1 ParFR, which further suggested a dominant elastomeric response to compression [38]. Furthermore, a higher elastic contribution allowing greater recovery could be accounted for a polymer matrix that is more flexible. On the other hand, if the rigid PF1 samples displayed dominant elastoplastic deformation, acting as homogenous solids on densification, they would be less able to recover [46].

3.5. Biodegradability

The end-of-life biodegradability of polymeric foams is a highly desirable property, as waste accumulation is mitigated and its reversion into biomass enhances its renewability. While it was noted that measuring mass loss may account for mechanisms of degradation other than microbial biodegradation alone, the use of controlled environments could mitigate the degree of influence of these factors. Furthermore, to minimize any potential damage to the specimen during cleaning for measurements, a small amount of soil was retained on the specimens. A mass loss of 0.34 ± 0.30% was measured for the negative control sample after 2 months in the laboratory environment, which suggested that processing of samples had a negligible contribution.

The mass loss as a function of time is plotted in Figure 13a for PF1 in both laboratory and natural soil burial environments. It was evident that rapid mass loss was achieved, which could be due to the hydrolytically susceptible ester bonds present on MACOG and hydrophilicity of the material promoting microbial colonization [79]. The rate of biodegradation was similar to MACO/styrene (30 wt%) foams as described by Wang et al. [22]. This result was surprising, since it was expected that MACOG/styrene would contain more elastically active chains than MACO/styrene (as previously indicated by Can et al. [25]), which was expected to decrease the rate of biodegradation [80]. Moreover, measurements by Wang et al. [22] were performed at 30 °C, and it is well-known that biodegradation rate increases with temperature [81]. Furthermore, the mass loss was higher than various AESO-based polymeric foams [12,14,17]. This result highlighted the potential of castor oil as a renewable feedstock compared to soybean oil-derived materials. Comparatively, it was interesting that there was no significant difference in mass loss between the two environments for the first three months (month 1: $p = 0.64$, month 2: $p = 0.55$, month 3: $p = 0.160$). Thereafter the laboratory environment was higher in month 4 ($p = 0.011$) but not significantly different after 5 months ($p = 0.076$), reaching 25.1 ± 0.6% and 23.2 ± 0.7% for the laboratory and natural environment, respectively.

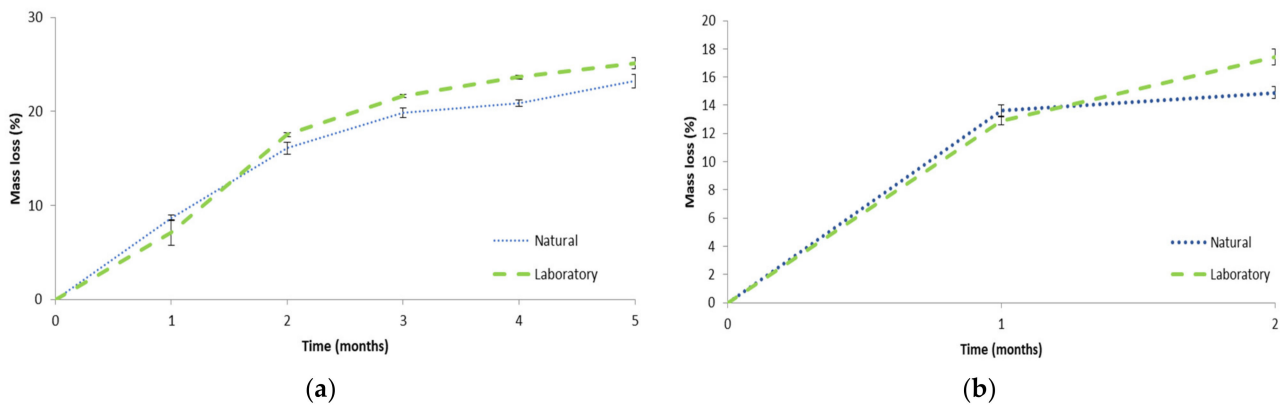

Figure 13. Mass loss of polymeric foam samples in natural and laboratory aerobic biodegradation conditions for (**a**) PF1 and (**b**) PF2.

The mass loss as a function of time was plotted in Figure 13b for PF2 in both laboratory and natural soil burial environments. The mass loss after 1 month was not significantly different between the two environments (p = 0.456), but in month two the laboratory environment was significantly higher than the natural environment (p = 0.019). After two months the mass loss for PF2 in the laboratory environment was significantly higher than PF1 month 2 in both the natural (p = 0.038) and laboratory (p = 0.019) environment. However, PF2 in the natural environment was not significantly different to PF1 month 2 in either the natural (p = 0.404) or laboratory (p = 0.806) environment. It was anticipated that PF2 may have a greater ability to biodegrade than PF1 owing to the hydrolytically susceptible ester bonds on the isobornyl fragments. However, as this was only observed for PF2 laboratory environment it could not be definitively ascertained whether the addition of IBOMA positively contributed to the biodegradability. Furthermore, it was acknowledged that longer biodegradation time for PF2 would be beneficial to try determining IBOMA's effect on the biodegradability.

SEM micrographs of the cell structure of polymeric foams after biodegradation are presented in Figure 14. Qualitatively, the formation of numerous erosion sites within the internal cellular structure could be observed, while the surface appeared to lose well-defined morphological integrity [22,82,83]. No obvious difference between the laboratory and natural samples could be identified from the images, suggesting that similar mechanisms of degradation occurred in both environments. The presence of small erosion sites within the cellular structure suggested that mass loss due to mechanisms other than mechanical degradation successfully took place, inferring that mass loss was likely due to microbial activity.

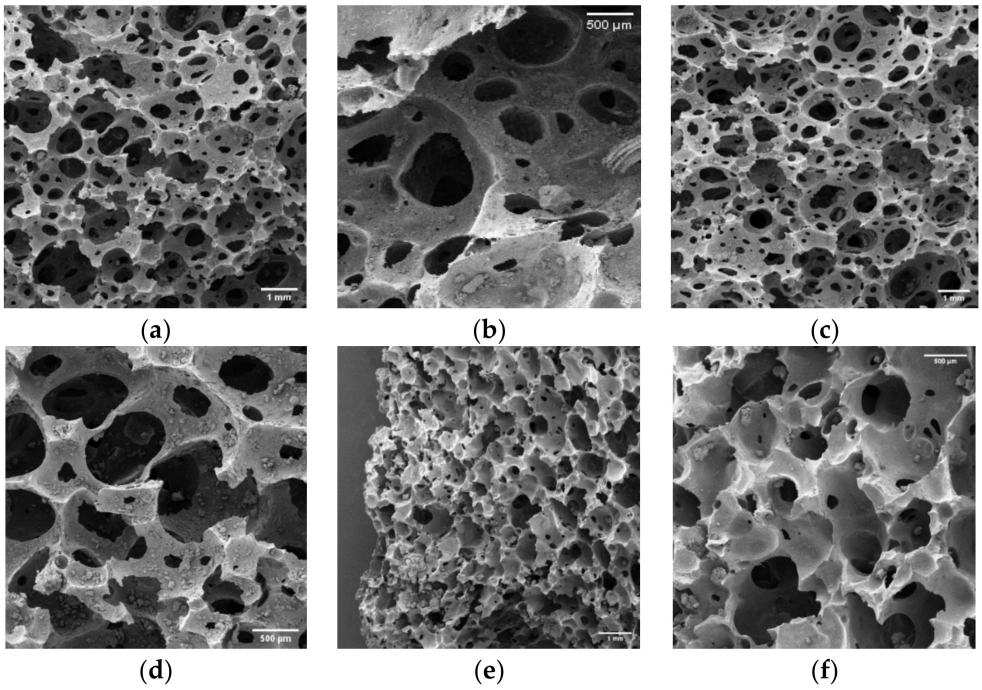

Figure 14. (**a**,**b**) PF1 after 5 months in a natural aerobic soil environment, (**c**,**d**) PF1 after 5 months in a laboratory aerobic soil environment, and (**e**,**f**) PF2 after 2 months in an aerobic soil environment.

4. Summary and Conclusions

This work demonstrated that renewable alternatives to petroleum-derived polymeric foams could be accomplished by using modified castor oil and isobornyl methacrylate as feedstocks. The synthesis of MACOG was achieved without the need for solvents or purification, thus providing an efficient and sustainable method of preparing a modified vegetable oil with suitable sites for free-radical polymerization. Furthermore, the carboxylic

acid groups on MACOG provided a convenient platform for foaming with $NaHCO_3$ as an environmentally benign foaming agent. While the preparation of polymeric foams by reactive foaming was not straightforward, some of the issues were resolved by optimizing the processing conditions to achieve consistent cell morphology. Furthermore, the degree of foaming could be tailored by the amount of $NaHCO_3$ employed, hence proving that a range of apparent density and porosity of polymeric foams were achievable with this method.

The resultant polymeric foams displayed anisotropic cell morphology with elongation in the direction of the foam rise and log-normal cell diameter distributions. Cell anisotropy was found to have a strong effect on the compressive properties of the polymeric foams, with improved properties in the direction of cell elongation, which was likely due to differing cellular deformation mechanics in either direction of the compression. This structure–property anisotropy can be exploited in design applications, although control over cell elongation would require further processing optimization. Furthermore, the compressive properties obeyed many other established cellular mechanical models, with structure–property relationships found related to the apparent density and average cell wall thickness. It was found that increasing apparent density was the dominant contributor to increased modulus and strength but decreased the ability to recover. The compressive energy absorption properties indicated that the foams could effectively absorb energy until the onset of densification. More specifically, the cellular structure of the polymeric foams influenced the ability to absorb energy, with greater strains at onset of densification and higher energy absorption efficiency for larger cell diameters. Additionally, the energy absorbed at the onset of densification was observed to increase with increasing apparent density. These relationship parameters provide valuable understanding toward controlling and tailoring the polymeric foams to provide suitable mechanical and energy absorption properties.

Overall, it was evident that both the polymer properties as well as morphological features influenced the compressive deformation mechanisms and hence mechanical and energy absorption properties. It also preemptively appeared that the processing conditions may have had an additional effect on the compressive properties. Comparatively, it was apparent that the choice of reactive diluent strongly influenced the mechanical properties of the polymeric foams. The sole employment of IBOMA as a reactive diluent was not successful in this work. It became apparent that careful consideration of both the relative reactivity of the functional groups and molecular structure of the reactive diluent was needed to provide effective hard segments within the polymer matrix to improve the overall mechanical properties. Indeed, the incorporation of IBOMA appeared to change the compressive cellular mechanics and thus the overall mechanical properties, which were generally lower than polymeric foams only using styrene. However, the energy absorption properties and recovery were comparable or higher than the polymeric foams only employing styrene, with exception to lower energy absorbed at the onset of densification. This work has provided an initial platform for understanding the incorporation of bio-based reactive diluents into VO-derived free-radically polymerized polymeric foams, which until now had not been reported in literature. That being said, the polymeric foams employing only styrene still provided a bio-based product that displayed favorable properties compared to many other bio-based polymeric foams reported in literature. Furthermore, all the polymeric foams displayed the ability to rapidly biodegrade in an aerobic soil environment, which allows for reversion to biomass at the end of lifespan, thus providing an environmentally sustainable material.

Supplementary Materials: The following are available online at https://www.mdpi.com/article/10.3390/polym13111872/s1, Figure S1: ^{1}H NMR spectra of (a) COG and (b) MACOG, Figure S2: ATR-FTIR spectra of castor oil (CO), glycerol (gly), COG, and MACOG, Table S1: ATR-FTIR peak assignments for castor oil (CO), glycerol, COG, and MACOG.

Author Contributions: J.A.D. and C.W. conceptualization; J.A.D. performed the experiments, formal analysis, data interpretation, and wrote the original draft.; C.W. supervised the work, acquired

funding, critically reviewed the manuscript, and approved the final version of the paper. All authors have read and agreed to the published version of the manuscript.

Funding: C.W. and J.A.D. would like to thank the University Research Committee of the University of Cape Town. J.A.D. would like to thank the Harry Crossley Research Fellowship, Vice Chancellor's Research Fellowship, Reino Stegen Scholarship, and University of Cape Town Postgraduate Funding Office.

Institutional Review Board Statement: Not applicable.

Informed Consent Statement: Not applicable.

Data Availability Statement: The data presented in this study are available on request from the corresponding author.

Conflicts of Interest: The authors declare no conflict of interest. The funders had no role in the design of the study; in the collection, analyses, or interpretation of data; in the writing of the manuscript, or in the decision to publish the results.

References

1. Islam, M.R.; Beg, M.D.H.; Jamari, S.S. Development of vegetable-oil-based polymers. *J. Appl. Polym. Sci.* **2014**, *131*. [CrossRef]
2. Kundu, P.P.; Das, R. Development of biobased polymers and their composites from vegetable oils. *J. Biodegrad. Biobased Polym. Environ. Biomed. Appl.* **2016**, 287–320. [CrossRef]
3. Miao, S.; Wang, P.; Su, Z.; Zhang, S. Vegetable-oil-based polymers as future polymeric biomaterials. *Acta Biomater.* **2014**, *10*, 1692–1704. [CrossRef]
4. Mustapha, R.; Rahmat, A.R.; Majid, R.A.; Mustapha, S.N.H. Mustapha, Vegetable oil-based epoxy resins and their composites with bio-based hardener: A short review. *Polym. Technol. Mater.* **2019**, *58*, 1311–1326.
5. Mustapha, S.N.H.; Rahmat, A.R.; Arsad, A. Bio-based thermoset nanocomposite derived from vegetable oil: A short review. *Rev. Chem. Eng.* **2014**, *30*, 167–182. [CrossRef]
6. Petrović, Z.S. Polyurethanes from vegetable oils. *Polym. Rev.* **2008**, *48*, 109–155. [CrossRef]
7. Tan, S.G.; Chow, W.S. Biobased epoxidized vegetable oils and its greener epoxy blends: A review. *Polym. Technol. Eng.* **2010**, *49*, 1581–1590. [CrossRef]
8. Galià, M.; de Espinosa, L.M.; Ronda, J.C.; Lligadas, G.; Cádiz, V. Vegetable oil-based thermosetting polymers. *Eur. J. Lipid Sci. Technol.* **2010**, *112*, 87–96. [CrossRef]
9. Sharma, V.; Kundu, P. Addition polymers from natural oils—A review. *Prog. Polym. Sci.* **2006**, *31*, 983–1008. [CrossRef]
10. Lu, P.; Guo, M.; Yang, Y.; Wu, M. Nanocellulose stabilized pickering emulsion templating for thermosetting AESO nanocomposite foams. *Polymers* **2018**, *10*, 1111. [CrossRef]
11. Sousa, A.F.; Ferreira, S.; Lopez, A.; Borges, I.; Pinto, R.; Silvestre, A.J.; Freire, C.S. Freire, Thermosetting AESO-bacterial cellulose nanocomposite foams with tailored mechanical properties obtained by Pickering emulsion templating. *Polymer* **2017**, *118*, 127–134. [CrossRef]
12. Bonnaillie, L.M. Bio-Based Polymeric Foam from Soybean Oil and Carbon Dioxide. Ph.D. Thesis, Department of Chemical Engineering, University of Delaware, Newark, DE, USA, 2007.
13. Bonnaillie, L.M.; Wool, R.P. Thermosetting foam with a high bio-based content from acrylated epoxidized soybean oil and carbon dioxide. *J. Appl. Polym. Sci.* **2007**, *105*, 1042–1052. [CrossRef]
14. Wu, S.P.; Qiu, J.F.; Rong, M.Z.; Zhang, M.Q.; Zhang, L.Y. Plant oil-based biofoam composites with balanced performance. *Polym. Int.* **2009**, *58*, 403–411. [CrossRef]
15. Rong, M.Z.; Zhang, M.Q.; Wu, S.P.; Wang, H.J.; Czigány, T. *Ecomaterials-Foam Plastics Synthesized from Plant Oil-Based Resins, Materials Science Forum*; Trans Tech Publications Ltd.: Zurich, Switzerland, 2007; pp. 2311–2316.
16. Lee, K.-Y.; Wong, L.L.C.; Blaker, J.; Hodgkinson, J.M.; Bismarck, A. Bismarck, Bio-based macroporous polymer nanocomposites made by mechanical frothing of acrylated epoxidised soybean oil. *Green Chem.* **2011**, *13*, 3117–3123. [CrossRef]
17. Qiu, J.F.; Zhang, M.Q.; Rong, M.Z.; Wu, S.P.; Karger-Kocsis, J. Rigid bio-foam plastics with intrinsic flame retardancy derived from soybean oil. *J. Mater. Chem. A* **2013**, *1*, 2533–2542. [CrossRef]
18. Campanella, A.; La Scala, J.J.; Wool, R.P. The use of acrylated fatty acid methyl esters as styrene replacements in triglyceride-based thermosetting polymers. *Polym. Eng. Sci.* **2009**, *49*, 2384–2392. [CrossRef]
19. Cousinet, S.; Ghadban, A.; Fleury, E.; Lortie, F.; Pascault, J.-P.; Portinha, D. Portinha, Toward replacement of styrene by bio-based methacrylates in unsaturated polyester resins. *Eur. Polym. J.* **2015**, *67*, 539–550. [CrossRef]
20. Yadav, S.K.; Schmalbach, K.M.; Kinaci, E.; Stanzione, J.F.; Palmese, G.R. Palmese, Recent advances in plant-based vinyl ester resins and reactive diluents. *Eur. Polym. J.* **2018**, *98*, 199–215. [CrossRef]
21. Yu, A.Z.; Serum, E.M.; Renner, A.C.; Sahouani, J.M.; Sibi, M.P.; Webster, D.C. Webster, Renewable Reactive Diluents as Practical Styrene Replacements in Biobased Vinyl Ester Thermosets. *ACS Sustain. Chem. Eng.* **2018**, *6*, 12586–12592. [CrossRef]

22. Wang, H.J.; Rong, M.Z.; Zhang, M.Q.; Hu, J.; Chen, H.W.; Czigány, T. Biodegradable foam plastics based on castor oil. *Biomacromolecules* **2007**, *9*, 615–623. [CrossRef]
23. Wang, H.J.; Zhang, C.Y.; Rong, M.Z.; Zhang, M.Q.; Czigány, T. Interfacial effects in short sisal fiber/maleated castor oil foam composites. *Compos. Interfaces* **2008**, *15*, 95–110. [CrossRef]
24. Can, E.; Wool, R.P.; Küsefoğlu, S. Soybean and castor oil based monomers: Synthesis and copolymerization with styrene. *J. Appl. Polym. Sci.* **2006**, *102*, 2433–2447. [CrossRef]
25. Can, E.; Wool, R.; Küsefoğlu, S. Soybean-and castor-oil-based thermosetting polymers: Mechanical properties. *J. Appl. Polym. Sci.* **2006**, *102*, 1497–1504. [CrossRef]
26. Echeverri, D.A.; Perez, W.A.; Rios, L.A. Synthesis of maleated-castor oil glycerides from biodiesel-derived crude glycerol. *Ind. Crop. Prod.* **2013**, *49*, 299–303. [CrossRef]
27. Echeverri, D.A.; Rios, L.A.; Rivas, B.L. Synthesis and copolymerization of thermosetting resins obtained from vegetable oils and biodiesel-derived crude glycerol. *Eur. Polym. J.* **2015**, *67*, 428–438. [CrossRef]
28. Campanella, A.; La Scala, J.J.; Wool, R.P. Fatty acid-based comonomers as styrene replacements in soybean and castor oil-based thermosetting polymers. *J. Appl. Polym. Sci.* **2010**, *119*, 1000–1010. [CrossRef]
29. ASTM. *Standard Test Method for Acid and Base Number by Color-Indicator Titration*; ASTM D974-14e2; ASTM International: West Conshohocken, PA, USA, 2014.
30. ASTM. *Standard Test Method for Determination of the Saponification Value of Fats and Oils*; ASTM D5558-95; ASTM International: West Conshohocken, PA, USA, 2017.
31. Huber, A.T.; Gibson, L.J. Anisotropy of foams. *J. Mater. Sci.* **1988**, *23*, 3031–3040. [CrossRef]
32. Shutov, F.A. Foamed Polymers. Cellular Structure and Properties. In *Industrial Developments*; Springer: Berlin/Heidelberg, Germany, 1983; pp. 155–218.
33. Aleksandrov, A.Y.; Borodin, M.Y.; Pavlov, V. *Constructions with Plastic Foam Fillers*; Mashinostroenie: Moscow, Russia, 1972. (In Russian)
34. ASTM. *Standard Test Method for Compressive Properties of Rigid Cellular Plastics*; ASTM D1621-16; ASTM International: West Conshohocken, PA, USA, 2016.
35. Li, Q.M.; Magkiriadis, I.; Harrigan, J.J. Compressive strain at the onset of densification of cellular solids. *J. Cell. Plast.* **2006**, *42*, 371–392. [CrossRef]
36. Tan, P.; Reid, S.; Harrigan, J.; Zou, Z.; Li, S. Dynamic compressive strength properties of aluminium foams. Part I—Experimental data and observations. *J. Mech. Phys. Solids* **2005**, *53*, 2174–2205. [CrossRef]
37. ASTM. *Standard Test Method for Determining Aerobic Biodegradation of Plastic Materials in Soil*; ASTM D5988-18; ASTM International: West Conshohocken, PA, USA, 2018.
38. Obi, B. *Polymeric Foams Structure-Property-Performance: A Design Guide*; William Andrew: Oxford, UK, 2017.
39. Shukla, S.; Agnihotri, S.; Pradeep, S.A.; Pilla, S. Delayed addition foaming of bio-epoxy blends: Balancing performance requirements and sustainability. *ACS Sustain. Chem. Eng.* **2018**, *6*, 17051–17058. [CrossRef]
40. Brown, N.F.; Pradeep, S.A.; Agnihotri, S.; Pilla, S. The power of processing: Creating high strength foams from epoxidized pine oil. *ACS Sustain. Chem. Eng.* **2017**, *5*, 8641–8647. [CrossRef]
41. Agnihotri, S.; Shukla, S.; Pradeep, S.A.; Pilla, S. Biobased thermosetting cellular blends: Exploiting the ecological advantage of epoxidized soybean oil in structural foams. *Polymer* **2019**, *177*, 111–119. [CrossRef]
42. Badía, A.; Movellan, J.; Barandiaran, M.J.; Leiza, J.R. High Biobased Content Latexes for Development of Sustainable Pressure Sensitive Adhesives. *Ind. Eng. Chem. Res.* **2018**, *57*, 14509–14516. [CrossRef]
43. Slone, R.V. Methacrylic Ester Polymers. *Encycl. Polym. Sci. Technol.* **2002**. [CrossRef]
44. Altuna, F.I.; Ruseckaite, R.A.; Stefani, P.M. Biobased thermosetting epoxy foams: Mechanical and thermal characterization. *ACS Sustain. Chem. Eng.* **2015**, *3*, 1406–1411. [CrossRef]
45. Mazzon, E.; Habas-Ulloa, A.; Habas, J.-P. Lightweight rigid foams from highly reactive epoxy resins derived from vegetable oil for automotive applications. *Eur. Polym. J.* **2015**, *68*, 546–557. [CrossRef]
46. Huang, X.; Yang, X.; Liu, H.; Shang, S.; Cai, Z.; Wu, K. Bio-based thermosetting epoxy foams from epoxidized soybean oil and rosin with enhanced properties. *Ind. Crop. Prod.* **2019**, *139*, 111540. [CrossRef]
47. Lau, T.H.; Wong, L.L.; Lee, K.-Y.; Bismarck, A. Tailored for simplicity: Creating high porosity, high performance bio-based macroporous polymers from foam templates. *Green Chem.* **2013**, *16*, 1931–1940. [CrossRef]
48. Gibson, L.J.; Ashby, M.F. *Cellular Solids: Structure and Properties*, 2nd ed.; Cambridge University Press: Cambridge, UK, 1999.
49. Chen, Y.; Das, R.; Battley, M. Modelling of closed-cell foams incorporating cell size and cell wall thickness variations. In Proceedings of the 11th World Congress on Computational Mechanics, Barcelona, Spain, 20–25 July 2014; pp. 20–25.
50. Nie, Z.; Lin, Y.; Tong, Q. Modeling structures of open cell foams. *Comput. Mater. Sci.* **2017**, *131*, 160–169. [CrossRef]
51. Gosselin, R.; Rodrigue, D. Cell morphology analysis of high density polymer foams. *Polym. Test.* **2005**, *24*, 1027–1035. [CrossRef]
52. Lautensack, C. Fitting three-dimensional Laguerre tessellations to foam structures. *J. Appl. Stat.* **2008**, *35*, 985–995. [CrossRef]
53. Wong, J.C.; Tervoort, E.; Busato, S.; Gonzenbach, U.T.; Studart, A.R.; Ermanni, P.; Gauckler, L.J. Macroporous polymers from particle-stabilized foams. *J. Mater. Chem.* **2009**, *19*, 5129–5133. [CrossRef]
54. Yin, D.; Xiang, A.; Li, Y.; Qi, H.; Tian, H.; Fan, G. Effect of Plasticizer on the Morphology and Foaming Properties of Poly(vinyl alcohol) Foams by Supercritical CO_2 Foaming Agents. *J. Polym. Environ.* **2019**, *27*, 2878–2885. [CrossRef]

55. Oliveira-Salmazo, L.; Lopez-Gil, A.; Silva-Bellucci, F.; Job, A.E.; Rodriguez-Perez, M.A. Natural rubber foams with anisotropic cellular structures: Mechanical properties and modeling. *Ind. Crop. Prod.* **2016**, *80*, 26–35. [CrossRef]
56. Tu, Z.; Shim, V.; Lim, C. Plastic deformation modes in rigid polyurethane foam under static loading. *Int. J. Solids Struct.* **2001**, *38*, 9267–9279. [CrossRef]
57. Thirumal, M.; Khastgir, D.; Singha, N.K.; Manjunath, B.S.; Naik, Y.P. Effect of foam density on the properties of water blown rigid polyurethane foam. *J. Appl. Polym. Sci.* **2008**, *108*, 1810–1817. [CrossRef]
58. Członka, S.; Sienkiewicz, N.; Kairytė, A.; Vaitkus, S. Colored polyurethane foams with enhanced mechanical and thermal properties. *Polym. Test.* **2019**, *78*, 105986. [CrossRef]
59. Marvi-Mashhadi, M.; Lopes, C.; Llorca, J. Effect of anisotropy on the mechanical properties of polyurethane foams: An experimental and numerical study. *Mech. Mater.* **2018**, *124*, 143–154. [CrossRef]
60. Bernardo, V.; Laguna-Gutierrez, E.; Lopez-Gil, A.; Rodriguez-Perez, M.A. Highly anisotropic crosslinked HDPE foams with a controlled anisotropy ratio: Production and characterization of the cellular structure and mechanical properties. *Mater. Des.* **2017**, *114*, 83–91. [CrossRef]
61. Kidd, T.; Zhuang, S.; Ravichandran, G. In situ mechanical characterization during deformation of PVC polymeric foams using ultrasonics and digital image correlation. *Mech. Mater.* **2012**, *55*, 82–88. [CrossRef]
62. Lim, G.; Altstädt, V.; Ramsteiner, F. Understanding the compressive behavior of linear and cross-linked poly (vinyl chloride) foams. *J. Cell. Plast.* **2009**, *45*, 419–439. [CrossRef]
63. Lee, J.-H.; Kim, S.-K.; Park, S.; Park, K.H.; Lee, J.-M. Unified constitutive model with consideration for effects of porosity and its application to polyurethane foam. *Compos. Part B Eng.* **2018**, *138*, 87–100. [CrossRef]
64. Sanders, W.; Gibson, L. Mechanics of hollow sphere foams. *Mater. Sci. Eng. A* **2003**, *347*, 70–85. [CrossRef]
65. Stengard, R. *Properties of Rigid Urethane Foams*; EI duPont de Nemours and Co.: Wilmington, NC, USA, 1963.
66. Stefani, P.; Barchi, A.T.; Sabugal, J.; Vazquez, A. Characterization of epoxy foams. *J. Appl. Polym. Sci.* **2003**, *90*, 2992–2996. [CrossRef]
67. Goods, S.; Neuschwanger, C.; Whinnery, L.; Nix, W. Mechanical properties of a particle-strengthened polyurethane foam. *J. Appl. Polym. Sci.* **1999**, *74*, 2724–2736. [CrossRef]
68. Song, C.; Wang, P.; Makse, H.A. A phase diagram for jammed matter. *Nature* **2008**, *453*, 629. [CrossRef] [PubMed]
69. Carriço, C.S.; Fraga, T.; Pasa, V.M. Production and characterization of polyurethane foams from a simple mixture of castor oil, crude glycerol and untreated lignin as bio-based polyols. *Eur. Polym. J.* **2016**, *85*, 53–61. [CrossRef]
70. Tondi, G.; Link, M.; Kolbitsch, C.; Gavino, J.; Luckeneder, P.; Petutschnigg, A.; Herchl, R.; van Doorslaer, C. Lignin-based foams: Production process and characterization. *BioResources* **2016**, *11*, 2972–2986. [CrossRef]
71. Liu, Y.; Rahimidehgolan, F.; Altenhof, W. Anisotropic compressive behavior of rigid PVC foam at strain rates up to 200 s^{-1}. *Polym. Test.* **2020**, *91*, 106836. [CrossRef]
72. Sousa, A.F.; Matos, M.; Pinto, R.J.; Freire, C.S.; Silvestre, A.J. One-pot synthesis of biofoams from castor oil and cellulose microfibers for energy absorption impact materials. *Cellulose* **2014**, *21*, 1723–1733. [CrossRef]
73. del Rosso, S.; Iannucci, L. On the compressive response of polymeric cellular materials. *Materials* **2020**, *13*, 457. [CrossRef] [PubMed]
74. Linul, E.; Şerban, D.-A.; Voiconi, T.; Marşavina, L.; Sadowski, T. Energy–absorption and efficiency diagrams of rigid PUR foams. *Key Eng. Mater.* **2014**, *601*, 246–249. [CrossRef]
75. Qiu, D.; He, Y.; Yu, Z. Investigation on compression mechanical properties of rigid polyurethane foam treated under random vibration condition: An experimental and numerical simulation study. *Materials* **2019**, *12*, 3385. [CrossRef]
76. Da Silva, V.R.; Mosiewicki, M.A.; Yoshida, M.I.; da Silva, M.C.; Stefani, P.M.; Marcovich, N.E. Polyurethane foams based on modified tung oil and reinforced with rice husk ash II: Mechanical characterization. *Polym. Test.* **2013**, *32*, 665–672. [CrossRef]
77. Koohbor, B.; Kidane, A. Design optimization of continuously and discretely graded foam materials for efficient energy absorption. *Mater. Des.* **2016**, *102*, 151–161. [CrossRef]
78. Saha, M.; Mahfuz, H.; Chakravarty, U.; Uddin, M.; Kabir, M.; Jeelani, S. Effect of density, microstructure, and strain rate on compression behavior of polymeric foams. *Mater. Sci. Eng. A* **2005**, *406*, 328–336. [CrossRef]
79. Woodard, L.N.; Grunlan, M.A. Hydrolytic degradation and erosion of polyester biomaterials. *ACS Macro Lett.* **2018**, *7*, 976–982. [CrossRef]
80. Huang, S.J.; Edelman, P.G. An overview of biodegradable polymers and biodegradation of polymers. *Degrad. Polym.* **1995**, 18–28. [CrossRef]
81. Pischedda, A.; Tosin, M.; Degli-Innocenti, F. Biodegradation of plastics in soil: The effect of temperature. *Polym. Degrad. Stab.* **2019**, *170*, 109017. [CrossRef]
82. Liszkowska, J.; Borowicz, M.; Paciorek-Sadowska, J.; Isbrandt, M.; Czupryński, B.; Moraczewski, K. Assessment of photodegradation and biodegradation of RPU/PIR foams modified by natural compounds of plant origin. *Polymers* **2019**, *12*, 33. [CrossRef]
83. Álvarez-Barragán, J.; Domínguez-Malfavón, L.; Vargas-Suárez, M.; González-Hernández, R.; Aguilar-Osorio, G.; Loza-Tavera, H. Biodegradative activities of selected environmental fungi on a polyester polyurethane varnish and polyether polyurethane foams. *Appl. Environ. Microbiol.* **2016**, *82*, 5225. [CrossRef] [PubMed]